Thermal Science and Engineering Progress 70 (2026) 104535

Contents lists available at ScienceDirect

Thermal Science and Engineering Progress

journal homepage: www.sciencedirect.com/journal/thermal-science-and-engineering-progress

Experimental and numerical analysis of water condensation in a condensing economiser for heat recovery☆

F. Orlandi [a], K. Račkaitis [b], L. Montorsi [a,*], R. Poškas [b], H. Jouhara [c]

[a] Department of Sciences and Methods for Engineering,University of Modena and Reggio Emilia, Via Amendola 2, Pad. Morselli - 42122 Reggio Emilia, Italy
[b] Nuclear Engineering Laboratory, Lithuanian Energy Institute, Breslaujos 3, LT-44403 Kaunas, Lithuania
[c] Heat Pipe and Thermal Management Research Group, College of Engineering, Design and Physical Sciences, Brunel University London, Uxbridge UB8 3PH, UK

ARTICLE INFO

Keywords:
Condensation
CFD
Heat Pipe Heat Exchanger
Multiphase

ABSTRACT

Condensing heat exchangers play a key role in industrial processes to enable high efficiency waste heat recovery. Various designs exist and they depend on the primary heat source, pollution level, installation location, etc. The physics involved in these components is very complex and usually difficult to investigate experimentally. Therefore, numerical methods, such as CFD (Computational Fluid Dynamics), prove to be a useful tool for investigating specific phenomena. In particular, the condensation phenomenon is probably the most complex since it implies the co-existence of different phases, their mutual interaction and the variations in concentration of these phases. Focusing on these phenomena, a simplified case study was conducted by considering an infinite pipe geometry and investigated by means of the STAR-CCM + software to develop a novel methodology for the detailed external condensation pro. The geometry considered represents the first tube section of an existing heat exchanger, and the condensation of hot humified air impinging on the cold pipe was analysed using a multiphase multicomponent approach based on VOF (Volume of Fluid Method). A specific optimum mesh was tested with two different flow regimes for the fluid film defined on the condensation surface. Since no condensation regime is known in advance, the Resolved Fluid Film model was used to trigger the condensation on the pipe wall, starting by means of the Fluid Film model, in order to predict the amount of condensate phase and its diffusion into the background region. After that, the VOF condensation model was used to trigger the condensation between the vapor phase and the newly formed water liquid phase. The condensation regime is then controlled by means of three main parameters being the two condensation models (film and VOF) under relaxation factors and the transition threshold, generally raging from 0 to 1 and here fixed to an optimal value. Finally, the total amount of condensate phase was compared with extrapolated values from experimental results. The simulation proved to be a reliable simplified prediction of the average condensation production related to the actual experimental setup, with the spatial distribution showing a net separation between the film and the VOF regimes.

1. Introduction

Over the years, computational fluid dynamics has proved to be a very powerful tool to be employed in different engineering/physics tasks. At the moment, the implementation of CFD spans many topics and industrial applications are among the most important. For example, its use can be cited in the characterization/investigation of industrial machines [1,2], specific components [3] and industrial processes [4,5]. Then, when arguing specifically about condensation/evaporation phenomena, the field varies quite widely, and sources of literature tend to do the same. For example, considering the theory per se, there are plenty of sources spanning from general two-phase topics [6], to specific physics formulations as the laminar film state [7] or even extensive investigations on specific heat transfer coefficient estimations[8,9]. When it comes to the topic of this simulation, it strongly depends on the field of interest. For example, some papers may focus on a specific topic like condensation applied to Internal Air Quality (IAQ) [10] or well investigated phenomena like various accident scenarios in the field of nuclear engineering [11,12,13]. In the first work from Mimouni et al. Makes use of the NEPTUNE solver to simulate the vapor condensation on a cooled surface based on two existing scenarios. The work from Zschaeck et al then validated a mathematical code implemented in Ansys FLUENT for wall condensation in presence of non-condensable gases. By

☆ This article is part of a special issue entitled: 'David Reay?s 80th' published in Thermal Science and Engineering Progress.

* Corresponding author.
E-mail address: luca.montorsi@unimore.it (L. Montorsi).

https://doi.org/10.1016/j.tsep.2026.104535
Received 31 October 2025; Received in revised form 16 December 2025; Accepted 24 January 2026
Available online 26 January 2026

Nomenclature

Abbreviation/Symbol

CFD	Computational Fluid Dynamic
VOF	Volume of Fluids
α	Volume Fraction
ρ	Density
$\boldsymbol{v}_{d,i}$	Diffusion Velocity
HIRC	High-Resolution Interface Capturing
$\dot{m}$	Condensation Rate
h_f	Film Thickness
u^+	Adimensional wall velocity
Re_{cr}	Critical Reynolds
Y_i	Vapor Mass Fraction
$\dot{m}_v$	Evaporation Rate
α_h	First Cell Volume Fraction
α_{trans}	Resolved Fluid Film Transfer Value
$\dot{m}$	Transfer Mass Flux
$f_{\sigma,n}$	Shear Stress Normal Component
$f_{\sigma,t}$	Shear Stress Tangential Component
τ_α	Fluid Film Shear Stress Tangential Component
f^D	Drag Force

implementing a mass sink the authors were to simulate a loss of coolant accident (LOCA). Finally, Li et al simulated direct contact condensation (DCC), a common phenomenon during accidents or transitions in nuclear reactors. The authors made use of the coupling of the LES turbulent model and VOF model with the addition of a UDF code introducing a mass transfer and an equilibrium model. Other topics are direct contact condensation, as for the work from Shukla et al [14], where steam condensation happens in a subcooled pool, or microchannel condensation as for Alnaimat et al [15] with a complete flow regime transition modelled. Turning to a topic more appropriate to the one discussed in this paper, heat exchangers, being the most important and simplest kind of application including condensation as a part of their operation, are a well-known technology, as easily ascertained by the work of Fujii [16]. Their easy conceptualization makes them a useful tool to be applied to a vast variety of cases spanning from heat recovery or even exhaust gas treatment. Some of the studies performed consider the evaluation of heat transfer coefficients, as for example the already cited work on the fluid film by Marto, or on the horizontal tube bundle from Browne [17]. When it comes to the use of CFD, the most part of the complex technologies studied have been demonstrated to be a valuable tool of investigation, and some interesting work can be found. One is surely the work from Ren et al [18], where, for an air/vapor stream in the presence of a bundle of horizontal tubes, a relationship was found between the percentage of non-condensable gases and the heat transfer coefficient. In the work from Lei et al [19], an interesting first numerical analysis was carried out for the condensation flow regimes in micro-channels, then with a later work [20] a computational investigation was conducted for condensation flow patterns and heat exchange in parallel rectangular micro-channels. Staying with the topic of internal condensation, another work that can be cited is from Mghari [21], with the use of the VOF multiphase model to simulate the annular condensation in a water-steam heat pipe. Khasawneh et al [22] investigated film condensation inside the Passive Auxiliary Feedwater System in nuclear safety systems. Also, Höhne [23] investigated the flow patterns of a functioning heat pipe, simulated by means of the homogeneous model. A very interesting study came from Bhowmilk [24,25], which in two subsequent publications reported by means of the fluid film model the condensation in scaled-down small modular reactors, first for pure steam and then for steam and non-condensable gases. Moving to external condensation, the topic of interest relevant to the present paper, Bonneau et al [26] published a review on vapor condensation outside smooth tubes, but it must be pointed out that the tubes were considered horizontal, in a single or bundle configuration, which effectively limits the general applicability of the work. Another similar case can be found in the review from Fil et al [27] on dropwise condensation, spanning theory, modelling and experiments. This demonstrates that condensation per se is a phenomenon that is extremely dependent on the environment and configurations of the surfaces where it happens. In the work from Lee et al [28] an interesting coupling between Star-CCM + and Mars-KS was brought forth to simulate the condensation on a wall in the presence of light gases, all experimentally validated by the CONAN data experiment. Unfortunately, this brief paper does not explain very much on the condensation models used. Then, a small portion of the work from Krackik [29] considered the implementation of CFD in the study for water/vapor condensation on the wall of a heat exchanger, but its use appears to be limited on the fields of motion.

For what the authors have acknowledged by investigating the literature, no previous effort was done in the simulation of the external vertical condensation process. Moreover, the condensation process is constituted by different passages that can be numerically implemented by means of different models, and as far as the authors know no effort was done in the coupling of different condensation models. Then, the present work aims to propose an in-depth analysis of water/vapor condensation on the external surface of a cooling pipe. The configuration is derived from an actual experimental heat exchanger from the work of Poškas et al [30]. The novelty of the proposed work arises from the coupling of different condensation models, with the result of a dynamic simulation between the film and the 3D condensed phase, all based on the gradient driven condensation/evaporation processes in Star-CCM + environment v. 18.06.007-R8, Siemens [31]. As stated before, no preceding studies on the external condensation were done with such a focus on the development of the condensation process. Starting from a dry wall, condensation on a portion of the original pipe, herein set with a constant heat transfer coefficient, the condensation process is brought forth to a statistically stationary condition and compared to a theoretical experimentally condensed phase volume.

2. Methodology

2.1. Actual technology

The present paper is based on a simplified analysis of a portion of a tube wall belonging to a heat exchanger designed at the Lithuanian Energy Institute (LEI) in collaboration with Brunel University London. The heat exchanger is composed of three longitudinal stainless-steel tubes of serpentine shape forming tube bundles, which are placed inside a rectangular stainless-steel frame. In these tubes the cooling water is flowed in counter-current in respect to the inlet gas stream. At the bottom of the steel case bottles are placed in correspondence with the lower curves of the tubes/pipes in order to collect condensate forming from the water vapor in the inlet stream.

In Fig. 1 a 3D model of the actual machine is given, with a detail of the internal bundles to the left. To this time the heat exchanger as already been tested in various experiments by Poškas et al. [30,32,33], all based on the condensation taking place on the external surface of the tubes bundle. Tests were performed with different inlet gasses (flue gasses from wooden pallets or biofuel combustions, humid air), different inlet temperatures (for both the gas and water currents) and gas/water ratios. All the experiments proved that condensation most of the times tales place due to the pipes wall temperature being below the gas dew point, with a different distribution along the pipes depending on the mass fraction of vapor in the gas stream.

2.2. Geometry

It must be pointed out that to treat such an extended domain with the

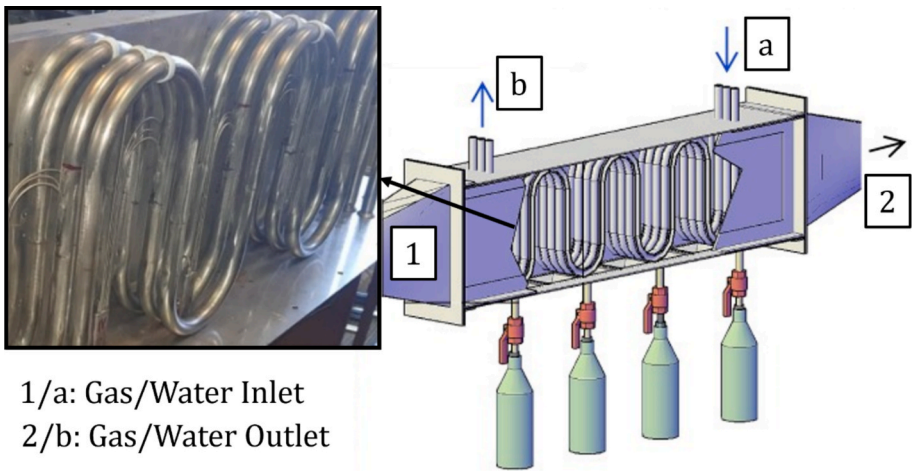

Fig. 1. Model of the heat exchanger with highlighted boundary conditions. Box shows a photo of the internal pipes.

aim of reproducing the condensation phenomenon would result in a thorough attempt with many detrimental challenges. So, as a first try to simulate the process, the original system was simplified. To simplify as much as possible, we focused our attention on just one vertical section of one of the tubes at the beginning of the impact of the incoming gas stream. As a further simplification, this vertical section is considered as fully symmetrical and is modelled ideally as an infinite tube, as shown in Fig. 2.

The model in Fig. 2 shows the boundaries and the dimensions of the reduced geometry. A and B are the Inlet and the Outlet surfaces respectively, while D and F are the top and the bottom surfaces. Finally, C is the pipe wall, identifiable by the lighter grey colour. The front and the back surfaces are not indicated but are easily identifiable. Since the actual heat exchanger is constituted by a bundle of three parallel pipes, this geometry is considered a half pipe section. This way the Front and Back surfaces are set as symmetric boundaries. The smaller side, i.e. the width of the Inlet and Outlet sections, corresponds to half of the distance between two parallel pipes. The top D and the bottom F walls are then set as symmetric periodic boundaries. By doing so the physical quantities passing through F will come back to the system by D, this way simulating an infinite pipe. The assumption of an infinite pipe is justified since this simplified case was meant to investigate a statistically stationary behaviour to be compared with the results of the actual machine in stable working conditions.

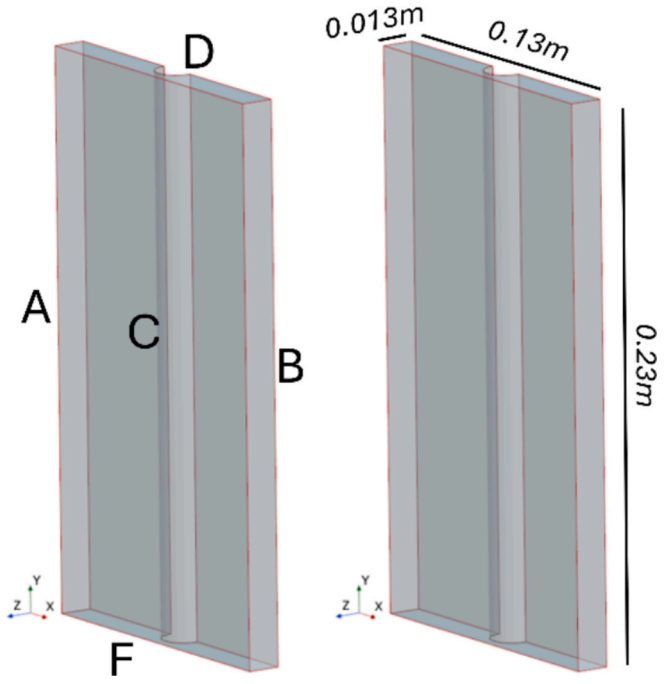

Fig. 2. Geometrical model for the infinite pipe with boundaries and dimensions.

2.3. Computational mesh

The whole mesh consisted of polyhedral elements. These kinds of cell were based on a first grid generated from all tetrahedral elements, which then collapsed into polyhedral elements and permitted high quality meshes (for example a polyhedral mesh always meets the non-orthogonality minimum requirements) with lower quantities of cells. This leads to more accurate results with a minor expense of computational time. Also, the polyhedral conformation adapts, in terms of the cells' quality, better to curvatures, for example the pipe boundary in the system. The generation of the mesh was done with the use of the *automated mesh method*, where the mesh is mostly handled by the software. The main parameter to be specified was the base cell dimension of 2.0 mm. Then the surface refinement to the pipe wall was specified as 25% of the base value.

The prism layer, to fulfil the stability requirements, consisted of 12 layers with a total thickness of 12.5% of the cell base. This operation is necessary since the prism layer has a fundamental role in this simulation due to the preferential orthogonal growing of the condensed phase thickness on the pipe wall. Also, to ensure the stability of multiphase simulations where a film condensation/evaporation is expected, it is generally advised to prefer a Low-y^+ behaviour on the condensation/evaporation surface. In Star-CCM + it is generally suggested the use of the All- y^+ wall treatment, which is the one employed here, and its nature (as it will be explained further in the next paragraph) is that of a blending model between the Low-y^+ and the High-y^+ ensuring an higher numerical stability. To ensure anyway a general Low-y^+ behaviour the wall-y + values on the pipe wall were checked to ensure that its values were below 1, while a negligible number of cells over 1 was accepted. The methodology applied to the mesh followed the optimization criteria for the condensation models [34,35,36]. The mesh was tested with a fluid-dynamic sensitivity applying two different fluid film motion models, one laminar and one turbulent. This way a mesh of ~ 5 thousand cells was obtained. Though it may seem too light it must be kept in mind that whenever phase density changes are computed the calculation time rises. Also, even slightly coarser meshes would result in a prompt divergence after few seconds of calculated physical time.

To perform a sensitivity analysis of the implemented mesh, two other meshes have been used by applying a coarsening factor of 1.5 and a

refining factor of 0.5 to the base size of the mesh in Fig. 3. In Fig. 4 the first result is shown in terms of the convolution lines for the velocity field in a transverse section achieved in half of the system. It can be seen that the motion varies slightly with minor differences, both in terms of shape and values.

In Fig. 5 another sensitivity comparison is shown, this time analyzing the pressure drop between inlet and outlet sections. The pressure field value was evaluated as surface average values on the sections' areas. The pressure drop between the two cases can be seen to be substantially identical with a negligible difference of 0.2 Pa. The two drops are also compared with the pressure drop with the selected mesh (green), showing that the value lies exactly beneath the two mesh testing values. It must be pointed out that Fig. 5 may be misled if interpreted only by using the relative pressure difference between the shown cases. By doing so, the relative pressure difference would reach 20% between the coarser and the finer case, thus supposing the adopted mesh to be unsatisfactory. It must be considered that experimentally a difference of 0.2 Pa is practically unquestionable. The results shown in Figs. 4-5 demonstrate the quality of the mesh generated thus validating its use for the present simulation.

2.4. Physics

The system is considered as being crossed by a hot stream of air and vapor. The stream impinges on the cold pipe wall and then the vapor component of the stream starts to condense on the pipe wall. The well-known Reynolds equations of continuity and momentum for a 3D system are implemented to simulate the physical phenomenon considered in the best way. Due to the incoming flowrate the Reynolds number is found to be fully turbulent, so that the implementation of a κ-ω SST model [37] was operated to fully resolve the turbulent behaviour both near and far from the wall boundary. The near-wall behaviour, necessary because of the turbulent flow models implemented, can generally be treated with two different methods. The first is the *High-y*$^+$, in which coarser near wall prism cells are used and the near wall cell is assumed to be fully lying in the log layer for $y^+>30$. In contrast, the second approach, named *Low-y*$^+$ assumed that the near wall cell lies in the viscous sub-layer, so finer prism cells are required since here $y^+\sim1$. Automatically, when selecting the turbulent models, Star-CCM + selects the All-y$^+$ which is fundamentally a blending model able to suit most of the grid dimensions in the near wall region. This model suits values of the wall-y + best so that $1 > y^+>30$. The values in between are ensured to be handled properly anyhow. Considering the mesh requirements in the previous section for the pipe wall and the use of this wall treatment instead of a *Low-y*$^+$, this let us use a classic κ-ω SST model instead of a low Reynolds version while maintaining the required refinement to the wall as demonstrated by the wall-y$^+$ values reported in Fig. 6.

2.4.1. VOF

The system is multiphase in nature, since the actual working scenario of the heat exchanger is the treatment of acidic exhaust gases from industrial processes. In the present simulation the incoming hot gas is simply treated as a bi-phase humid gas, consisting of a mixture of air and water vapor. To model the multiphase nature of the gas, use was made of the VOF model [38]. The VOF method is based on the use of a so-called colour function that leads to the definition of the volume fraction

$$\alpha_i = \frac{V_i}{V} \tag{1}$$

where V_i is the volume of a single phase and V is the total volume. The fundamentals of the volume fraction α_i are that the sum of all the i-phases are equal to 1, i.e. equal to the total volume of the system, and that the values of the single volume fraction in a grid cell can assume all the values between 0 and 1. It is important to note that within the VOF formulation the phases are considered as immiscible. Specifically, for 0 the cell is void of the volume fraction and for 1 the cell is filled with the volume fraction. The distribution of the phase i is driven by the phase mass conservation equation

$$\frac{\partial}{\partial t}\int_V \alpha_i dV + \oint_A \alpha_i \boldsymbol{v} \bullet d\boldsymbol{a} = \int_V \left(S_{\alpha_i} - \frac{\alpha_i}{\rho_i}\frac{D\rho_i}{Dt}\right)dV - \int_V \frac{1}{\rho_i}\nabla \bullet \left(\alpha_i \rho_i \boldsymbol{v}_{d,i}\right)dV \tag{2}$$

where on the left hand side the time and convective terms are described and put equal to the variation of the densities of the phases in the first term on the right hand side, described by the difference between the source term for the phase *i* with S_{α_i} and the Lagrangian derivative of the phase densities $D\rho_i/Dt$, and the contribution of the diffusive term exploited by the diffusion velocity $\boldsymbol{v}_{d,i}$. Anyway, since the diffusion term derives from the slip between the phases and since air and vapour can be assumed to have equal velocities, this term is zero. In Star-CCM+, in the case of a two-phase system, as in the present case, the phase volume fractions are calculated based on the resolution of the volume fraction transport equation for the first phase only. The volume fraction of the second phase is then adjusted correspondingly to the calculated values for the first phase, so that the sum of both the volume fractions leads to 1, that represents the totality of the cell volume. The VOF methodology belongs to the interface reconstruction methods, and in the present case the standard HIRC (High-Resolution Interface Capturing) method was used for this purpose. Since the system ideally starts from a condition where the heat exchanger chamber is filled with only air, the condensation process is likely to follow the wall pipe condensation process starting from a dry wall initial condition. The condensation process should follow the formation of nucleation sites on the dry wall surface dependent on the impinging of the hot humid gas on the pipe wall itself. These nucleation sites will then coalesce with each other after their own growth in dimension, forming in the end a homogeneous fluid film on the surface. The progression of this process will then lead to the forming of three-dimensional waves with the growth of the fluid film due to the continuous condensation on its own surface. This three-dimensional condensed liquid, not anymore classifiable as a film, will then further develop collecting on the bottom of the system dragged by the gravity force. The final shape of the condensate in the system will be the result of the combined effect of the drag force exercised by the gas stream flowing around the pipe surface and the surface tension between the condensate surface and the gas in the background.

In Star-CCM + the whole condensation process described above must be implemented with the use of different models all coupled. The

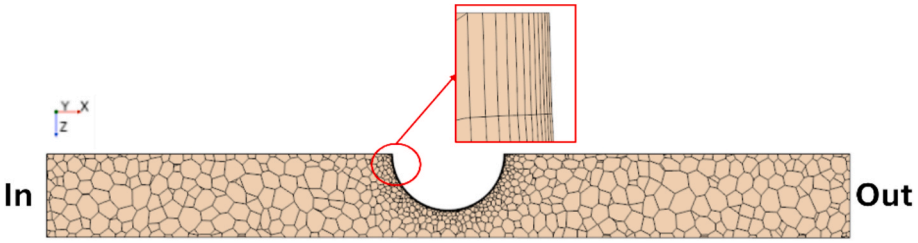

Fig. 3. Computational mesh in along a horizontal section.

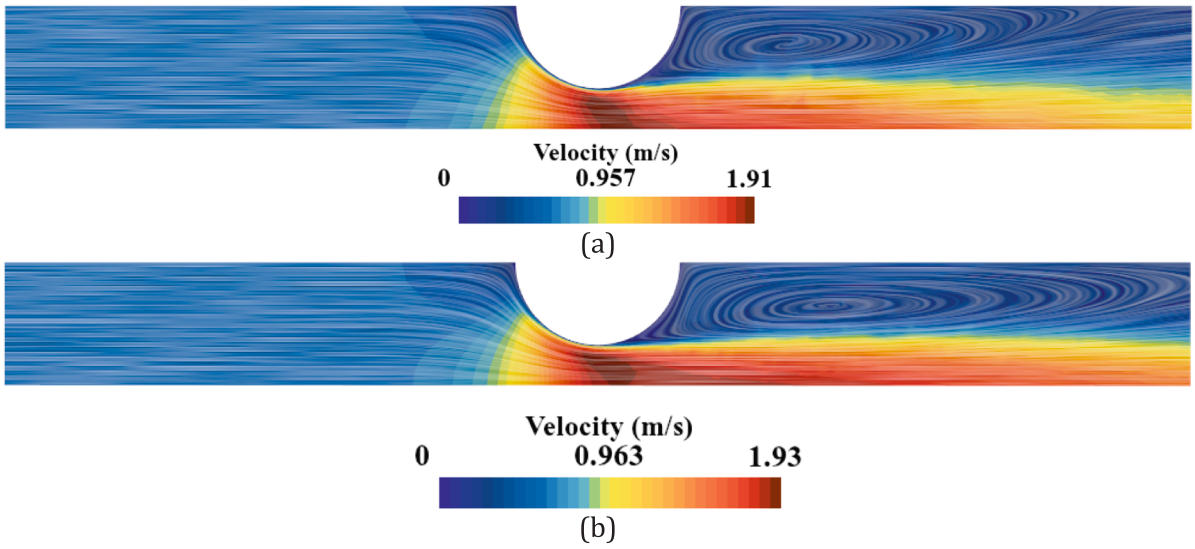

Fig. 4. Velocity convolution lines in a transvers section for (a) a coarser mesh and (b) a finer mesh.

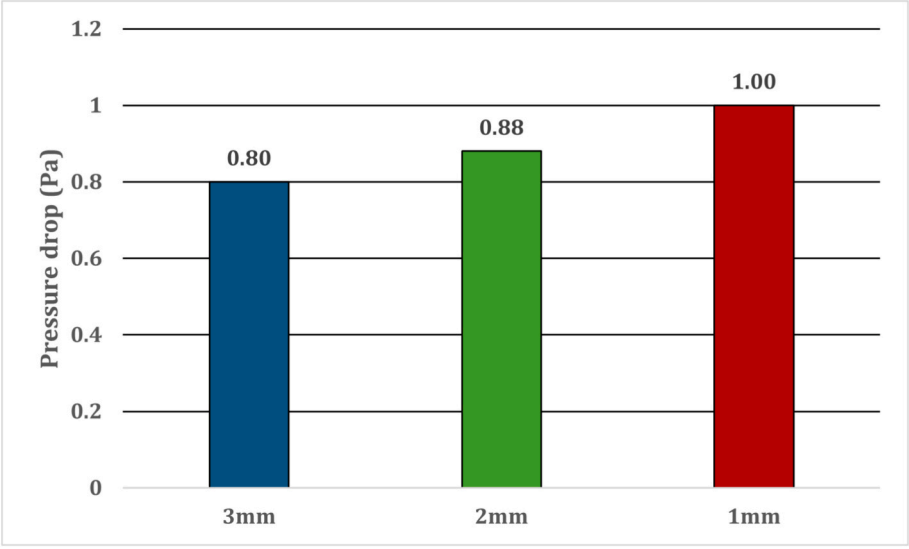

Fig. 5. Pressure drop between inlet and outlet sections for the coarser (blue), standard (green) and finer (orange) cases. (For interpretation of the references to colour in this figure legend, the reader is referred to the web version of this article.)

process then can be divided into steps as follows.

1. Definition of the VOF air/vapour mixture stream, that will form the background region
2. Generation of the Fluid Film due to the impinging of the VOF mixture on the pipe wall
3. Development of a 3D VOF liquid phase and corresponding condensation of the vapour phase on it

Along with the equations (1)-(2) the condensation process in the VOF multiphase model is based on the assumption that both evaporation and condensation are hydrodynamically limited, that is the driving force is the diffusion of species happening at the free surface interface to which the species are in equilibrium. The condensation rate for the phase i, at the interface, is defined as

$$\dot{m}_i = -\frac{\rho_g D_{g,i} \frac{\partial Y_{g,i}}{\partial n}\Big|_s}{1 - \sum_j^N Y_{g,j}^S} \tag{3}$$

where D_g is the diffusion coefficient and Y^s the component mass fraction. It can be seen that the condensation is calculated to happen mainly in the normal direction, which is shown by the normal derivative of the mass fraction at the numerator. This justifies the importance of using higher prism layers to ensure sufficient precision for the condensed component to be resolved along the surface of interest. As can be seen, energy doesn't come into play for the VOF condensation model.

2.4.1.1. Fluid film. The *Fluid Film* model was then implemented to simulate the formation of the fluid film itself, acting as the first step of the condensation process. This model makes use of a custom surface named *shell region* which in the present case is going to be defined as coherent with the pipe wall. This region is then interfaced with the background VOF region and gives rise to the formation of the fluid film itself after the interaction with the air/vapour phase. The formation of the fluid film is regulated by its own mass conservation equation

$$\frac{\partial}{\partial t}\int_V \rho_f dV + \int_A \rho_f \boldsymbol{v}_f \bullet d\boldsymbol{a} = \int_{\boldsymbol{v}} \frac{S_u}{h_f} dV \tag{4}$$

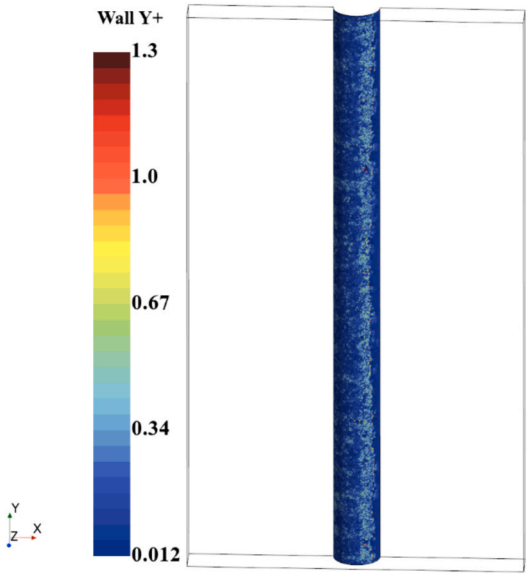

Fig. 6. Wall-y^+ values on the pipe wall.

where the resolution of this equation leads to the calculation of the fluid film thickness h_f. Alongside eq. (4) are the momentum, energy and species mass conservation equations. Since the flowing gas is simulated in turbulent conditions, the same is done for the fluid film. The turbulent fluid film model solves for the wall shear stress and the film surface velocity. For these two the following definition is used

$$u^+ = \begin{cases} y^+ & 0 < y < h_{pm} \\ \frac{1}{2}\ln(y^+) + C & h_{pm} < y < \delta \end{cases} \tag{5}$$

where k, C are constants, δ represents the fluid film thickness, h_{pm} is the film thickness corresponding to the point of intersection between the two parts of the equation and y is the coordinate in the normal direction to the film flow direction. Additionally, the turbulent viscosity model solves for the thermal conductivity and mass diffusivity. The model herein implemented is the *Mudawwar model* [39] that was formulated for films moving under gravity effects, that are regulated by the following equation

$$\frac{\mu}{\mu_t} = \sqrt{1 + K^2 y^{+2} \times \left(1 - \frac{y^+}{\delta^+}\right)^2 \times \left[1 - exp\left(-\frac{y^+}{26} \times \left(1 - \frac{y^+}{\delta^+}\right)^{1/2}\right) \times \left(1 - \frac{0.865 Re_{crit}^{0.5}}{\delta^+}\right)\right]^2} \tag{6}$$

where K is a constant, Re_{crit} the critical Reynolds number. For this latter parameter, two formulations are at disposal for the form $Re_{crit}^{0.5}$, one in the case of heating and one for evaporation/condensation. With the present case mainly focused on the condensation/evaporation, the calculation of the critical Reynolds number will be defined as $Re_{crit}^{0.5} = 0.04/K_a^{0.38}$, with K_a being the Kapitza number defined as $(\mu^4\rho)/(\rho\sigma^3)$. This model fundamentally develops a profile for the ratio μ/μ_t fitted to the bulk region of the film, for which data derive from the work of Ueda [40]. The same profile is then modified with a Van Driest damping function with the final form as equation (6).

When condensation comes into play, the vapour pressure of each component depends on the concentration of the component itself in the mixture. Linked to the vapour pressure is the evaporation rate, so that, for each component the mass flux conservation at the gas/film interface leads to

$$\rho Y_i\left(v - \dot{h}\right) - \rho D_i \frac{dY_i}{dy} = \rho_f Y_{f,i}\left(v_f - \dot{h}\right) - \rho_f D_{f,i} \frac{dY_{f,i}}{dy}\bigg|_f \tag{7}$$

where to the left is the gas side and to the right the film side. The term v is the normal component of the velocity and $\dot{h}$ the change of rate of the film thickness, so that the first term of each difference depends on convective terms and the second on diffusive terms. Equation (7) is valid below saturation conditions. Combined with the total mass flux conservation (dependent only on the $v - \dot{h}$ term), it is possible to obtain a formulation of the vapour mass fraction Y_i (dependent on Raoult's Law for the partial pressures) so that the evaporation rate for each component can be expressed as

$$\dot{m}_{v,i} = -\rho_f \dot{h} Y_i - \rho D_i \frac{dY_i}{dy} \tag{8}$$

where $-\rho_f \dot{h} = \dot{m}_v$, and it is assumed that the species distribution in the fluid film is constant. Equation (8) is valid for condensation too, for which it is enough to change the sign, and which is valid for all conditions. Apart from the hydrodynamic effects described by the previous equations the fluid film evaporation/condensation can be influenced also by thermal effects. This contribution is taken in account by combining equation (8) with an interfacial heat flux leading to the expression for the total evaporation rate

$$\dot{m}_v = \frac{\dot{Q}_v + \sum_i^{N_v} \Delta H_i^{vap} \rho D_i \frac{dY_i}{dy}}{\sum_i^{N_v} \Delta H_i^{vap} \rho D_i \frac{dY_i}{dy}} \tag{9}$$

where $\dot{Q}_v$ is the evaporation heat flux defined as $\sum_i^{N_v} \Delta H_i^{vap} \dot{m}_{v,i}$ and H_i^{vap} the evaporation enthalpy for the i phase.

2.4.1.2. Resolved fluid film model. To take in account the progression of the condensation process that leads to the evolution of a 3D liquid phase from the fluid film, use is made of the *Resolved Fluid Film* model. This model permits the passage from a bidimensional surface of the fluid film to a 3D liquid phase in the VOF background region. Given the interface grid cell, its volume fraction is calculated as

$$\alpha_h = \frac{V_{VOF} + V_{film}}{V_{cell}} \tag{10}$$

where V_{VOF} is the volume of the VOF phase, V_{film} the volume of the film phase and V_{cell} the volume of the cell itself. At this point a threshold value α_{TRANS} is defined, with values between 0 and 1, so that for 1 the cell is filled with a VOF phase and for 0 it is filled with a film phase. The values of α_h are constantly compared to that of α_{TRANS} so that two cases are possible.

- $\alpha_h > \alpha_{TRANS}$, then the film phase is converted in a VOF phase
- $\alpha_h < \alpha_{TRANS}$, then the VOF phase is converted in a film phase

For both cases the mass flux from one phase to the other is regulated by

$$\dot{m} = (\alpha_h - \alpha_{TRANS}) \bullet \frac{\widetilde{m}}{\tau} \tag{11}$$

where $\widetilde{m}$ is the phase mass available to be transferred and τ is the

time scale of the order of the timestep. The sign for equation (11) is positive for *film→VOF* transfers, i.e. the first case above. As shown in the work of Jouhara et al [41], the effect of the surface tension is a mandatory parameter to be taken into account for a realistic behaviour of bi-phase systems. The effect of the surface tension is implemented for both the VOF and the film regions. For both regions the surface tension is divided into the normal and the tangential components, but the definitions are slightly different for each component. The normal component for the VOF is defined as

$$f_{\sigma,n} = \sigma\kappa\boldsymbol{n} = -\sigma\nabla \bullet \left(\frac{\nabla\alpha_i}{|\nabla\alpha_i|}\right)\nabla\alpha_i \tag{12}$$

where σ is the surface tension coefficient, κ the mean curvature of the free surface and $\boldsymbol{n}$ the normal vector to the surface. The second form derives from the continuum surface force (CSF) model [42] for which the normal vector can be defined as $\boldsymbol{n} = \nabla\alpha_i$. For the film then it is defined as

$$f_{\sigma,n} = p_\sigma\boldsymbol{n} = -a\sigma\left(\nabla_s^2 h_f\right)\boldsymbol{n} \tag{13}$$

where p_σ is the capillary pressure, a is a non-dimensional scale factor and $\nabla_s^2 h_f$ approximates the surface curvature of the liquid surface. Moving to the tangential component, the VOF region is defined as

$$f_{\sigma,t} = \frac{\partial\sigma}{\partial t}t = (\nabla\sigma)_t|\nabla\alpha_i| \tag{14}$$

where t is the unit vector in the tangential direction to the free surface. The second form is obtained similarly for equation (12) with the CSF model. This term becomes important when the surface tension coefficient varies along the surface, for example due to temperature differences. For the fluid film the definition is as follows

$$\tau_\sigma = b\sigma(1-\cos\theta)\nabla\omega \tag{15}$$

where b is an empirical parameter, ω is 1 if $h_f > h_{f,min}$ (with the latter arbitrarily chosen by the user) and 0 elsewhere and finally θ is the contact angle.

The last element to be taken into account is the pressure variation in the fluid film due to the gas streamlines over its surface. The net force resulting from this is called Drag Form Force. This is defined by the same name model with the addition of the following equation

$$f^D = C_D\frac{\rho}{2}\boldsymbol{v}^2 A \tag{16}$$

where C_D is the drag coefficient and A is the cross-sectional area between the flowing gas and the fluid film. This equation is added to the momentum equation of the fluid film, while it is neglected for the gas phase.

The working scheme in Fig. 7 summarizes the coupling of the implemented models for the condensation process. Starting from (1) the air/vapor mixture enters the system, but since initially there is no VOF water phase it follows (2). In (2) the film condensation process is shown.

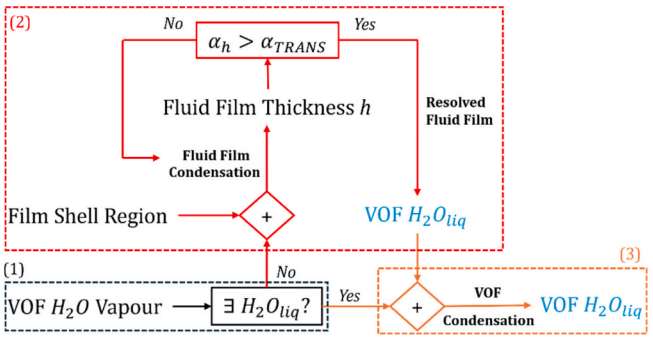

Fig. 7. Working scheme for the condensation process.

In the beginning the VOF vapor interacts with the film shell region and the film thickness is developed through the condensation process as the combination of equations (8)-(9) leading to the calculation of h with means of equation (4). Then, while the fluid film thickness varies during the film condensation process it is checked if the condition required by the resolved fluid film ($\alpha_h > \alpha_{TRANS}$) is met. In the beginning of the process the result is more likely to give way to no, so the film condensation progresses. With the development of the calculation the fluid film thickness h is expected to reach a value for which $\alpha_h > \alpha_{TRANS}$ is obtained, so the resolved fluid film model generates a VOF liquid phase regulated by equation (9). At this point the condition requested by the black rectangle in (1) is met, so the VOF vapor phase can condensate on the newly formed VOF liquid phase (3) by means of equation (3).

2.5. Physical domain and boundary conditions

As previously stated, the proposed methodology aims to simulate the external pipe wall condensation in the simplified infinite tube configuration, derived from an actual heat exchanger. The gas stream is modelled as a VOF mixture composed of air and vapor, respectively 0.9 and 0.1 of the total mass fractions. The gas enters with an initial temperature of 85°C and 17 kg/s, with the outlet section defined as a pressure outlet. The gas mass flow was derived from the turbulent mass flow profile of the complete system, appropriately scaled with the ratio of the reduced flow cross-sectional area and the wider original one. The pipe, as shown in Fig. 2, is void of any coolant fluid flowing inside it. To replicate the actual heat transfer the pipe wall was simulated with a convection thermal specification that specifies the convection thermal flux across the boundary in W/m^2. With this specification is possible to specify a Heat Transfer Coefficient, herein chosen as being 600 W/m^{2}K, which is an average value perfectly suitable for most applications regarding heat exchangers [43]. Based on the Courant number the timestep was set as 0.7 ms. It can be argued that the selected size is surely inadequate to properly simulate density phase changes in this case, but this is based on a numerical stability strategy that aims to maintain "high" timestep sizes combined with stronger stabilization techniques, such as the use of the SIMPLEC algorithm instead of the standard SIMPLE algorithm, a finer AMG solver convergence criterion. To further stabilize the simulation, the heat of formation shift technique was adopted, where the heat of formation energy is all shifted to the water phase in the fluid film or the VOF phase, and put to 0 for the vapor phase. Physically it corresponds to assigning all the heat of formation only to one of the two component phases in the condensation process. By doing so the heat of formation for the water phases is set to −2240 kJ/kg. For the fluid film then, the initial conditions were set basically as for an initially dry wall, so the initial thickness is put equal to zero. The initial dry wall approach is meant to stabilize the calculation in the first seconds where the wall is defined as perfectly dry since the fluid film is still to be formed. To do so the nucleation density is raised reasonably with values that can be varied between 10^6-10^{12} /m^2 (where obviously the higher the nucleation density the higher the condensation output). Unfortunately, these values should be evaluated by experimental results, but since it is not always possible to obtain such parameters, an empirical value is frequently used to properly set up the condensation/evaporation intensity to reach the expected experimental results. In the present case, a maximum value of 10^{12} /m^2 for the nucleation density was fixed. Various investigations shown that values below 10^{10} /m^2 would always produce an insufficient condensate quantity, so the maximum value was chosen. By doing so the simulation was assured to be stabilized in the first dry wall moments and if the output would result in an exceeding production of condensation, it could be simply tuned by means of the under-relaxation factors (URF). Also, by proceeding with the fixation of the parameters with the most uncertainty derived by the amplitude of the interval of values the URFs of the condensation models (film and VOF) become the sole tuning controls of the process. The simulation was run on a supercomputer with 9 core and 468 logical

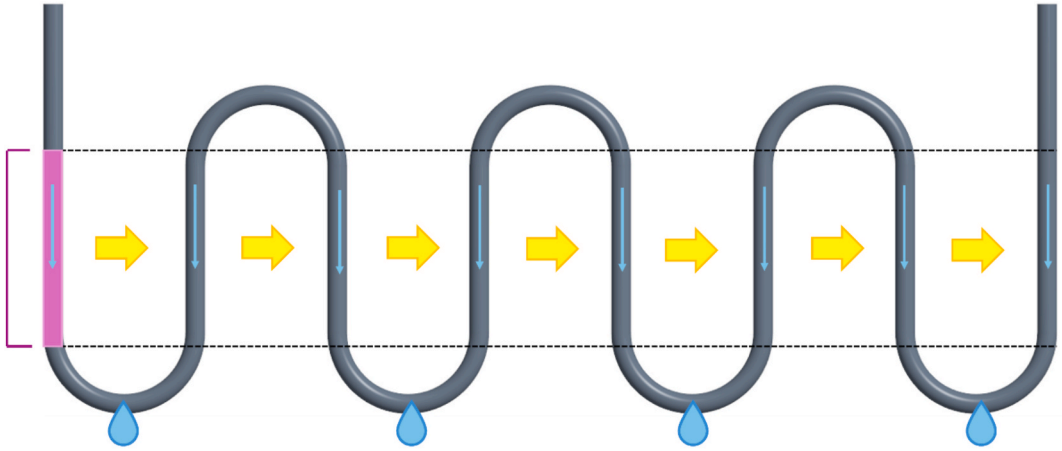

Fig. 8. Simplified scheme of the condensation on an actual pipe and the geometry of the reference section for the present paper.

processors, and the simulation was run for approximately 48 h until a statistically stationary condition was met.

2.6. Validation of the results

To validate the results from the simulation data average values of the condensed water collected were calculated based on the actual geometry. In Fig. 8 the actual pipe geometry is shown. It must be noted that in the actual heat exchanger three parallel pipes are employed as shown in Fig. 1. To be clearer the pipe shown in Fig. 8 is the central pipe visible in the inside of the CAD model on the right of Fig. 1.

The reference section in pink, corresponding to the vertical section of the simulated geometry, is indicated as the first feature of the pipe on the path of the hot air/vapour stream. The hot stream is represented in Fig. 8 with the yellow arrows. Also, the condensation scheme is evidenced in a simplified manner. As already explained in the previous Physics subsection, condensation starts by forming on the vertical tubes. Once the condensed water is sufficiently heavy gravity draws it down, in the actual geometry collecting on the lower curves. Once the condensed volume is sufficient it detaches from the surface by forming a drop and it is collected at the bottom of the geometry. During 60 s of the working period the actual heat exchanger produced a total of 0.17 L. From the ideal hypothesis of a homogeneous distribution of the condensate production on one of the three pipes, the value of 4.5 mL is found for one single vertical section. This value is considered as the target to which the results are going to be compared.

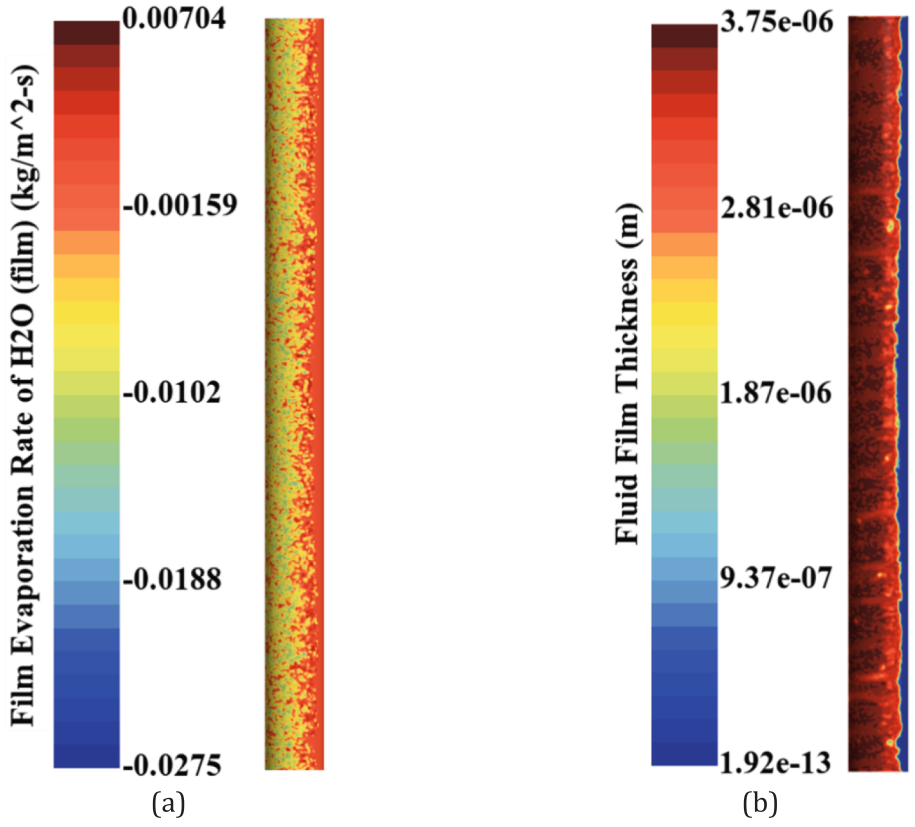

Fig. 9. Evaporation Rate (a) and Thickness (b) for the fluid film.

3. Results and discussion

The results shown in this paragraph were all obtained after a statistically stationary condition was recognized, and so the simulation was stopped after 120 s. The results herein presented are divided between the fluid film results, referring to the shell region calculations, and then on the background results, which means all the results that refer to the VOF region correspond to the volume shown in Figs. 2-3, where the condensed water phase can be traced. Finally, the condensed water phase, namely the VOF liquid phase, is characterized in terms of temporal behaviour and the quantity collected over a period of 60 s is compared with the experimental results.

The two main results of interest for the fluid film region are reported in Fig. 9. In (a) the condensation/evaporation rate is shown. Since in Star-CCM + the Evaporation Rate works for both condensation and evaporation, the sign distinguishes between the two. In this case the evaporation zones (>0) are neglectable and confined to very small spots on the right, which may be identified by the dark red colour. Otherwise, the condensation rate (<0) covers the whole shell region. Referring to the values in the label, the left side is characterized by higher values of condensation rate that tend to a lower progression to the right side. From this it can be deduced that the film is produced by the condensation of the vapor impinging on the pipe's surface on the left side, being the side of the impingement, while on the right the red shade corresponds more or less to a null rate. Moving to Fig. 9 (b) the fluid film thickness is reported. First, the thickness per se in the vertical configuration is very small of the order of micrometres with the highest thickness of 3.75e-6 m. The distribution of the film is easily identified, being all concentrated on the left side. Contrary to the scalar rate figure in (a), the fluid thickness label shows that the fluid film is not homogeneously distributed on the left side but presents a rough distribution, where traces of shear forces due to the flowing gas are easily identifiable, being lighter in colour.

In Fig. 10 then we move to the connection between the film and the VOF regions. As pointed out in the theory section, to develop a 3D condensed water phase starting from the fluid film it is necessary to make use of the *Resolved Fluid Film* model. Here the transfer of the phase is regulated by the α_{TRANS} threshold value. The passage between the phases can be traced by the definition of a threshold of the same value of α_{TRANS} by means of the volume fraction quantity. The result shown in Fig. 10 is this threshold. It shows that the water VOF phase develops from all the surface of the pipe, with the exclusion of some spots on the left side that correspond exactly to the fluid film portions. This relation becomes obvious when remembering equation (10), that states which can exist at the same instant in the first cell on the shell-background interface can be only one of the two models, VOF or Film.

While the threshold result in Fig. 10 provides an idea of the generation of the VOF liquid phase, it is not sufficient to locate the phase itself. So, in Fig. 11 the volume fraction for the liquid water is reported, with a little transparency to show the internal values, since a 3D visualization of the volume fraction would render everything with the superficial low values of the volume fraction itself. A detail is also reported for the upper corner of the condensed phase where the narrow depth of the water VOF phase is easily seen, that doesn't exceed 0.9 mm. Similar to the threshold, and coherently with the fluid film results, the volume fraction distribution is substantially concentrated on the right side, while on the left side few spots with a low concentration of water are visible.

To further investigate the axial asymmetry of the distribution of the condensed phases, the velocity field is investigated. In Fig. 12 a cross section of the velocity field is reported. Here is clearly visible the high gradient that forms in correspondence of the top of the pipe's curve. This strong velocity gradient, along with the effect of the convective shear stress generated by the flowing gas onto the pipe is believed to lead to the asymmetrical distribution of the phases, with the film on the left and the VOF on the right.

Finally, the VOF water phase mass was monitored to validate the present simulation with data at disposal from the experiment The reason behind the mass tracking instead of a volume tracking is due to the numerical uncertainties that may affect the volumes. This may happen when rapid phase densities change in small portions of the system, while mass monitoring instead is assured by means of the fulfilling of the

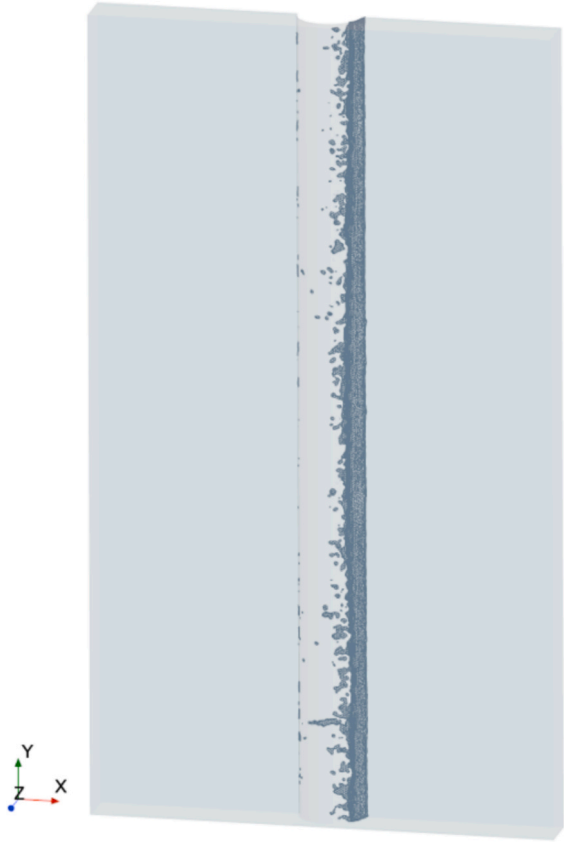

Fig. 10. Communication threshold for..α_{TRANS} = 0.1

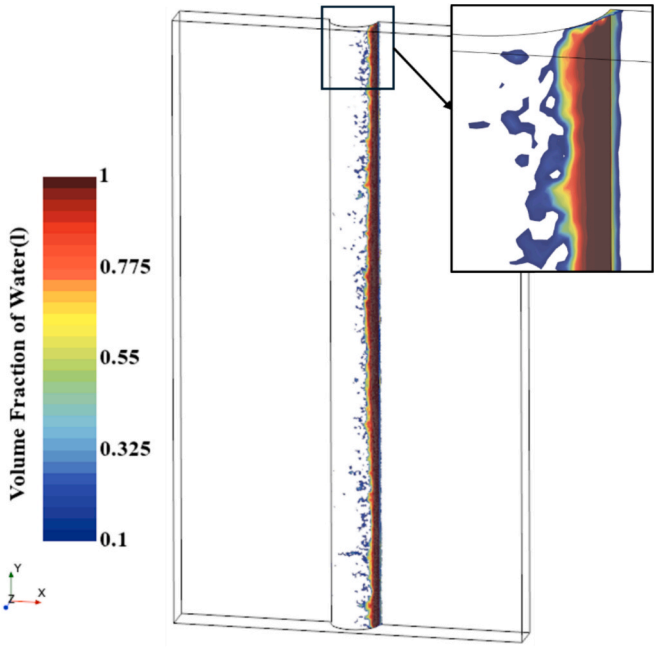

Fig. 11. Volume Fraction of the condensed water.

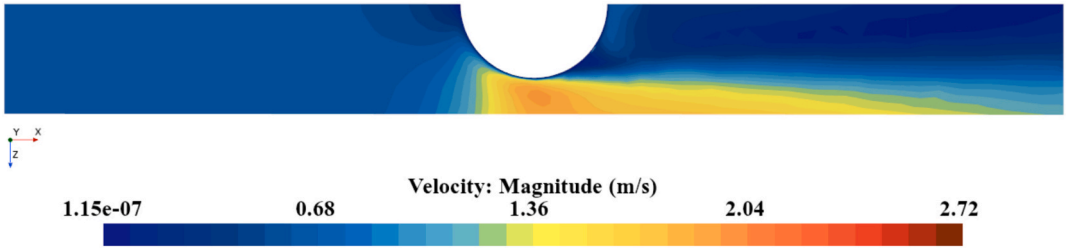

Fig. 12. Velocity field on the xz plane.

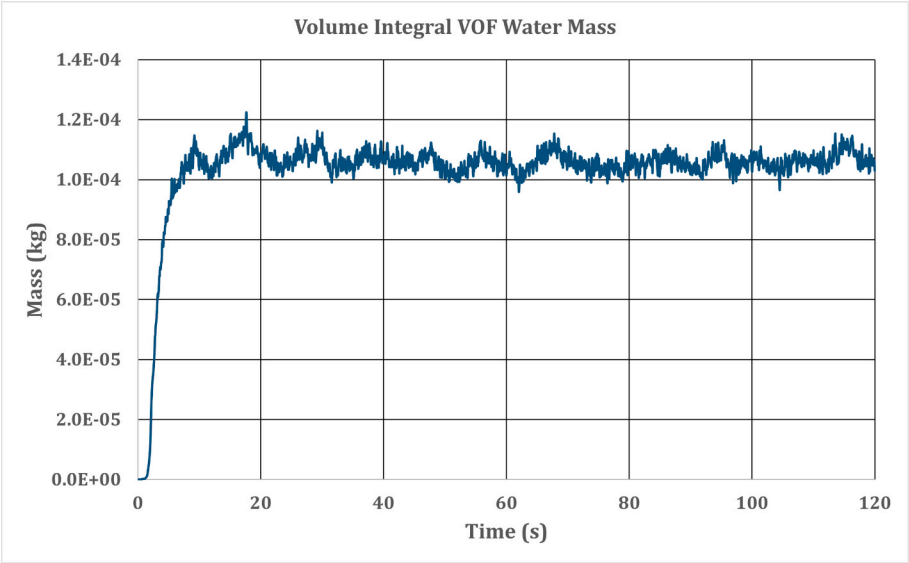

Fig. 13. Water Mass.

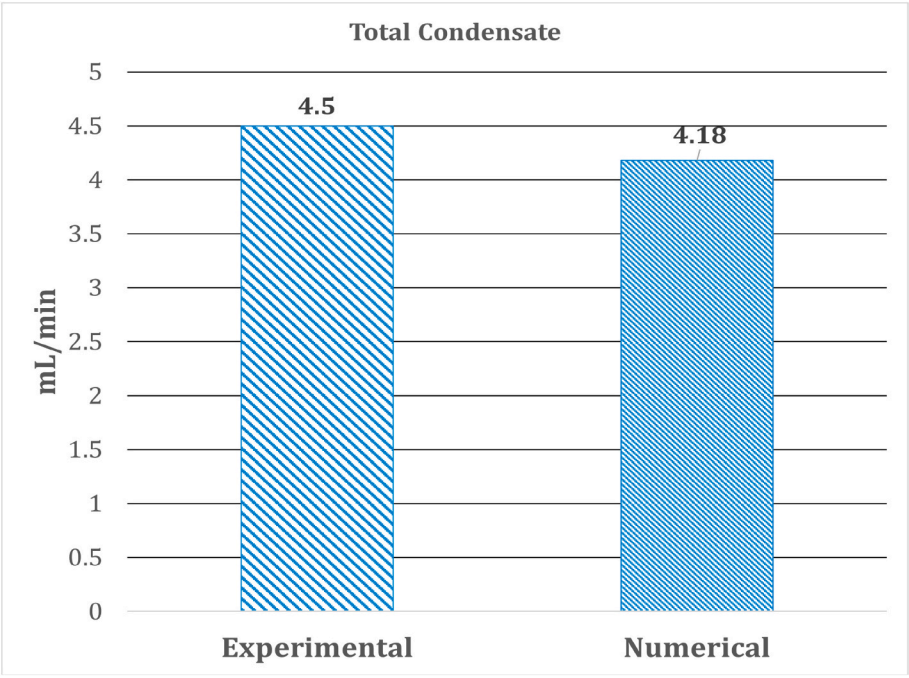

Fig. 14. Comparison between the condensate numerical prediction (left) and the experimental value (right).

continuity equation. Fig. 13 then shows the evolution of the condensed water VOF phase. The monitoring was realized by the volume integral of the following expression

$$Y_{water} \bullet \rho_{water} \bullet \alpha_{water} \tag{17}$$

where Y_{water} is the mass fraction of water, needed to identify the phase defined in the multi-component liquid (1 in this case being all water), ρ_{water} the density of the water phase and α_{water} the volume fraction of the water phase. The water phase appears around 1.3 s of simulation and rises until it reaches the order of 0.1 mg. Then it oscillates, being always confined in the 0.1–0.12 mg range. This behaviour is maintained stably all the way during the simulated time. These oscillations indicate that there is a dynamic equilibrium between the fluid film and the VOF water phase, where the evaporation phenomenon is not taken into account due to its very small values and the negligible spots visible in Fig. 9 (a).

From the experimental usage of the actual heat exchanger, 0.17 L/min of collected water is estimated for a whole working day. From this, dividing by the vertical sections and the curves (each corresponding to approximately half of a vertical section length), a value of 4.5 mL/min is obtained. This theoretically corresponds to the vertical section used in this paper. To obtain the calculated mL/min via simulation the following formula has been used

$$\frac{\overline{m}_{wat}}{t} \bullet 60 \tag{18}$$

where $\overline{m}_{wat}$ is the average liquid water mass [kg], t the cycle period [s] and 60 is the conversion to minutes. The temporal portion corresponds to a 60 s time period along the plot in Fig. 13 during the statistically stationary period.

The comparison between the experimental value, obtained as mentioned in the "Validation of Results" subparagraph, and the numerical prediction is shown in the bar plot in Fig. 14. As previously mentioned the experimental value was obtained as an average value considering a 60 s time of nominal functioning of the heat exchanger, which led to the value of 4.5 mL/min. The numerical value was then obtained by applying equation (18), and this led to the value of 4.18 mL/min. By comparing the two values an underestimation of 7% in respect to the experimental values is reported.

4. Conclusions

In the present paper the external condensation on a pipe was investigated by developing a novel CFD methodology in Star-CCM + for a detailed condensation process. The geometry was obtained from a symmetrical simplification of an actual vertical section of a cooling pipe from an existing heat exchanger. The incoming hot gas was characterized as a multiphase mixture with mass fractions of 0.9 for air and 0.1 for water vapor using the VOF multiphase model. The pipe was simplified with a constant heat transfer coefficient. The overall condensation process is the result of the coupling of three different models, each simulating a different step of the wall condensation in a vertical configuration.

The overall results can be summarized as follows.

- The fluid film is found to form specifically at the left side of the pipe, i.e. the first part of the pipe on which the hot gas mixture impinges. The fluid film instead of a homogeneous distribution on the wall shows signs of dragging to the right side due to the gas flow. The maximum film thickness obtained was in between of 3 to 4 μm.
- The Resolved Fluid Film model generates the water phase effectively. Its role is made evident by the threshold *iso*-surface (as shown in Fig. 9), where the threshold *iso*-surface is generated being equal to the transitional volume fraction.
- The condensed phase, coherently with the transitional *iso*-surface, accumulates mainly on the right side of the pipe wall. This phenomenon is found to be linked with the velocity field of the gas stream, where the flow along the surface of the pipe evidently breaks the fluid film surface homogeneity.
- The VOF water phase starts being created around 1.3 s and rises until it reaches the 0.1 mg order of magnitude. Then the mass monitoring shows a dynamic oscillation that endures for all the simulated 120 s. These oscillations, always confined in the 1.0–1.2 mg range, are small in entity and their repetition shows the reaching of a statistically stationary condition.
- The comparison with the experimental estimation shows that instead of the expected 4.5 mL/min a value of 4.18 mL/min was obtained, thus reporting an error of 7%.

The methodology presented is demonstrated to be a valuable tool to predict the condensation process on the outside of a pipe wall, and as far as the authors know, represents also a novelty in the literature of condensation in heat exchangers. With the small difference in terms of the calculated condensed phase, in future work other condensation models may be implemented, specifically those models that rely on temperature gradients instead of only concentration gradients as with the VOF condensation model. This way, the difference (although low) may be corrected. Also, the use of other multiphase models may be used to investigate the detachment of the condensed phase by means of a model that may include droplet modelling, as for example the dispersed phase model, even though this would require a different methodology method apart from the VOF model which is the one implemented here. Finally, the extension to an actual case, maybe the complete heat exchanger geometry will be a task to fulfil to move onto a better agreement between simulated and experimental data. In this case topics of interest will surely be the spatial distribution of the condensation models, to investigate if they agree with the experimental data. Finally, the possibility to implement the fluid film condensation model to be linked in a cross region heat transfer condition such as the liquid – pipe – gas case of a condenser is a topic to be investigated.

CRediT authorship contribution statement

F. Orlandi: Writing – original draft, Visualization, Validation, Software, Resources, Methodology, Investigation, Formal analysis, Data curation. **K. Račkaitis:** Validation, Methodology, Formal analysis. **L. Montorsi:** Supervision, Funding acquisition, Conceptualization. **R. Poškas:** Supervision, Project administration, Conceptualization. **H. Jouhara:** Supervision, Funding acquisition, Conceptualization.

Declaration of competing interest

The authors declare that they have no known competing financial interests or personal relationships that could have appeared to influence the work reported in this paper.

Acknowledgment

The paper was supported by the European Union's Horizon 2020 funded project iWAYS (the grant agreement No 958274). Additional information about the project is available at: iWays—Water closed loop in industrial processes—iWays.

Data availability

The data that has been used is confidential.

References

[1] M. Milani, L. Montorsi, M. Venturelli, A combined numerical approach for the thermal analysis of a piston water pump, International Journal of Thermofluids 7–8 (2020), https://doi.org/10.1016/j.ijft.2020.100050.

[2] A. Rezvanpour, R.E. Miller, Scaling analysis as a tool to validate CFD simulation of a lubricant flow in the bearing housing of a gas turbine, Therm. Sci. Eng. Prog. 36 (2022), https://doi.org/10.1016/j.tsep.2022.101513.
[3] J.V.M.B. de Siqueira, M.A.P. Rosa, G.B. Ribeiro, Three-dimensional CFD investigation of a scramjet inlet under different freestream conditions, Therm. Sci. Eng. Prog. 27 (2022), https://doi.org/10.1016/j.tsep.2021.101051.
[4] M. Milani, L. Montorsi, G. Storchi, M. Venturelli, CFD analysis and experimental measurements of the liquid aluminum spray formation for an Al–H2O based hydrogen production system, Int. J. Hydrogen Energy 46 (59) (2021) 30615–30624, https://doi.org/10.1016/j.ijhydene.2021.01.119.
[5] T. Zadravec, B. Rajh, F. Kokalj, N. Samec, CFD modelling of air staged combustion in a wood pellet boiler using the coupled modelling approach, Therm. Sci. Eng. Prog. 20 (2020), https://doi.org/10.1016/j.tsep.2020.100715.
[6] S. Manservisi, R. Scardovelli, *Termoidraulica dei flussi bifase*, Società Editrice Esculapio (2012).
[7] T. Fujii, U. Haruo, Laminar Filmwise Condensation on a Vertical Surface, International Journal of Heat Mass Transfer 15 (1972) 217–233.
[8] P.J. Marto, Film condensation heat transfer measurements on horizontal tubes: problems and progress, Exp. Therm Fluid Sci. 5 (1992) 556–569.
[9] C. Mao, Y. Su, CFD based heat transfer parameter identification of greenhouse and greenhouse climate prediction method, Therm. Sci. Eng. Prog. 49 (2024), https://doi.org/10.1016/j.tsep.2024.102462.
[10] J. Liu, H. Aizawa, H. Yoshino, "CFD prediction of surface condensation on walls and its experimental validation", in: Building and Environment, Elsevier BV, 2004, pp. 905–911, 10.1016/j.buildenv.2004.01.015.
[11] S. Mimouni, A. Foissac, J. Lavieville, CFD modelling of wall steam condensation by a two-phase flow approach, Nucl. Eng. Des. (2011) 4445–4455, https://doi.org/10.1016/j.nucengdes.2010.09.020.
[12] G. Zschaeck, T. Frank, A.D. Burns, CFD modelling and validation of wall condensation in the presence of non-condensable gases, Nucl. Eng. Des. 279 (2014) 137–146, https://doi.org/10.1016/j.nucengdes.2014.03.007.
[13] S.Q. Li, P. Wang, T. Lu, CFD based approach for modeling steam-water direct contact condensation in subcooled water flow in a tee junction, Prog. Nucl. Energy 85 (2015) 729–746, https://doi.org/10.1016/j.pnucene.2015.09.007.
[14] S.K. Shukla, A.M.N. Samad, S. Ghosh, CFD simulation of steam condensation in a subcooled water pool, Therm. Sci. Eng. Prog. 2 (2017) 80–86, https://doi.org/10.1016/j.tsep.2017.04.006.
[15] F. Alnaimat, K. El Kadi, B. Mathew, CFD investigation of R134a and propane condensation in square microchannel using VOF model: Parametric study using steady state solution, Therm. Sci. Eng. Prog. 38 (2023), https://doi.org/10.1016/j.tsep.2023.101662.
[16] T. Fujii, U. Haruo, History of Steam Condensers. (1988).
[17] M.W. Browne, P.K. Bansal, An overview of condensation heat transfer on horizontal tube bundles, Appl. Therm. Eng. 19 (1999) 565–594.
[18] B. Ren, L. Zhang, H. Xu, J. Cao, Z. Tao, Experimental study on condensation of steam/air mixture in a horizontal tube, Exp. Therm Fluid Sci. 58 (2014) 145–155, https://doi.org/10.1016/j.expthermflusci.2014.06.022.
[19] Y. Lei, Z. Chen, Numerical study of condensation flow regimes in presence of non-condensable gas in minichannels, Int. Commun. Heat Mass Transfer 106 (2019) 1–8, https://doi.org/10.1016/j.icheatmasstransfer.2019.04.001.
[20] Y. Lei, I. Mudawar, Z. Chen, Computational and experimental investigation of condensation flow patterns and heat transfer in parallel rectangular micro-channels, Int. J. Heat Mass Transf. 149 (2020), https://doi.org/10.1016/j.ijheatmasstransfer.2019.119158.
[21] H. El Mghar, R. El Amraoui, H. Grimech, Z. Ishane, M. Mouqallid, Annular condensation CFD models for the water-steam in the heat pipe systems, Journal of Materials Ans Environmental Science 8 (3) (2017) 763–771.
[22] K. Khasawneh, Y.H. Jeong, Indirect validation of fluid-to-fluid scaling criteria for modeling steam condensation based on empirical correlations and CFD simulations, Nucl. Eng. Des. 378 (2021), https://doi.org/10.1016/j.nucengdes.2021.111235.
[23] T. Höhne, CFD simulation of a heat pipe using the homogeneous model, International Journal of Thermofluids 15 (2022), https://doi.org/10.1016/j.ijft.2022.100163.
[24] P.K. Bhowmik, J.P. Schlegel, V. Kalra, S.B. Alam, S. Hong, S. Usman, CFD validation of condensation heat transfer in scaled-down small modular reactor applications, part 1: pure steam, Exp Comput Multiph Flow 4 (4) (2022) 409–423, https://doi.org/10.1007/s42757-021-0115-5.
[25] P.K. Bhowmik, J.P. Schlegel, V. Kalra, S. Alam, S. Hong, S. Usman, CFD validation of condensation heat transfer in scaled-down small modular reactor applications, part 2: Steam and non-condensable gas, Exp Comput Multiph Flow 4 (4) (2022) 424–434, https://doi.org/10.1007/s42757-021-0113-7.
[26] C. Bonneau, C. Josset, V. Melot, B. Auvity, "Comprehensive review of pure vapour condensation outside of horizontal smooth tubes", Elsevier Ltd, 2019, 10.1016/j.nucengdes.2019.04.005.
[27] B. El Fil, G. Kini, S. Garimella, "A review of dropwise condensation: Theory, modeling, experiments, and applications", Elsevier Ltd, 2020, 10.1016/j.ijheatmasstransfer.2020.120172.
[28] C.W. Lee, J.-S. Yoo, H.K. Cho, "Heat structure coupling of MARS-KS and STAR-CCM + for wall condensation in the presence of non-condensable gases containing light gas", in: *Transactions of the Korean Nuclear Society Autumn Meeting Goyang*, Goyang, 2019, pp. 24–25.
[29] P. Kracík, F. Toman, J. Pospísil, S. Kraml, A heat exchanger with water vapor condensation on the external surface of a vertical pipe, Energies (basel) 15 (15) (2022), https://doi.org/10.3390/en15155636.
[30] R. Poškas, A. Sirvydas, L. Mingilaitė, H. Jouhara, P. Poškas, Experimental investigation of water vapor condensation from flue gas in different rows of a heat exchanger model, Therm. Sci. Eng. Prog. 47 (2024), https://doi.org/10.1016/j.tsep.2023.102365.
[31] "Simcenter STAR-CCM+ 2310 - User Guide," *Siemens PLM Software*: 2310.0001 (18.06.007). Accessed: Dec. 27, 2024. [Online]. Available: https://plm.sw.siemens.com/en-US/simcenter/fluids-thermal-simulation/star-ccm/.
[32] R. Poškas, A. Sirvydas, M. Salem, P. Poškas, H. Jouhara, Experimental investigation of water vapor condensation from hothumidified air in serpentine heat exchanger, Int. J. Heat Mass Transf. 221 (2024), https://doi.org/10.1016/j.ijheatmasstransfer.2023.125068.
[33] R. Poškas, A. Sirvydas, M. Salem, P. Poškas, H. Jouhara, Experimental investigation of humidified air condensation in different rows of serpentine heat exchanger – Cooling water flow rate effect, Thermal Science and Engineering Process 54 (2024), https://doi.org/10.1016/j.tsep.2024.102814.
[34] S. Hardt, F. Wondra, Evaporation model for interfacial flows based on a continuum-field representation of the source terms, J. Comput. Phys. 227 (11) (2008) 5871–5895, https://doi.org/10.1016/j.jcp.2008.02.020.
[35] A. Cioncolini, J.R. Thome, C. Lombardi, Algebraic turbulence modeling in adiabatic gas-liquid annular two-phase flow, Int. J. Multiph. Flow 35 (6) (2009) 580–596, https://doi.org/10.1016/j.ijmultiphaseflow.2009.02.002.
[36] C. Bai and A. D. Gosman, "Mathematical Modelling of Wall Films Formed by Impinging Sprays," *JOURNAL OF ENGINES*, vol. 105, pp. 782–796, 1996, [Online]. Available: https://www.jstor.org/stable/44736317.
[37] F.R. Menter, Two-equation eddy-viscosity turbulence models for engineering applications, AIAA J. 32 (8) (1994) 1598–1605, https://doi.org/10.2514/3.12149.
[38] C.W. Hirt, B.D. Nichols, Volume of Fluid (VOF) method for the dynamics of free boundaries, Journal of Computational Physics 39 39 (1981) 201–225, https://doi.org/10.1016/0021-9991(81)90145-5.
[39] I.A. Mudawwar, M.A. El-Masri, Momentum and heat transfer across freely-falling turbulent liquid films, Int. J. Multiphase Flow 12 (5) (1986) 771–790.
[40] H. Ueda, R. Mueller, S. Komori, T. Mizushina, W. We, Eddy diffusivity near the free surface of open channel flow, Int J. Heat Transfer 20 (1977) 1127–1136.
[41] H. Jouhara, B. Fadhl, L.C. Wrobel, Three-dimensional CFD simulation of geyser boiling in a two-phase closed thermosyphon, Int. J. Hydrogen Energy 41 (37) (2016) 16463–16476, https://doi.org/10.1016/j.ijhydene.2016.02.038.
[42] J.U. Brackbill, D.B. Kothe, C. Zemach, A continuum method for modeling surface tension*, J. Comput. Phys. 100 (1992) 335354.
[43] Engineering Toolbox, "Heat Exchangers - Overall Heat Transfer Coefficients," https://www.engineeringtoolbox.com/heat-transfer-coefficients-exchangers-d_450.html. Accessed: Feb. 08, 2025. [Online]. Available: https://www.engineeringtoolbox.com/heat-transfer-coefficients-exchangers-d_450.html.